Materials Science & Engineering A 893 (2024) 146129

Contents lists available at ScienceDirect

Materials Science & Engineering A

journal homepage: www.elsevier.com/locate/msea

The dispersion-strengthening effect of TiN evoked by *in situ* nitridation of NiCu-based Alloy 400 during gas atomization for laser powder bed fusion

J.-P. Roth [a,*], I. Šulák [b], Z. Chlup [b], J. Fischer-Bühner [c], U. Krupp [d], K. Jahns [a]

[a] Faculty of Engineering and Computer Science, Osnabrück University for Applied Sciences, 49076, Osnabrück, Germany
[b] Institute of Physics of Materials, Czech Academy of Sciences, 61600, Brno, Czech Republic
[c] INDUTHERM Erwärmungsanlagen GmbH, 75045, Walzbachtal, Germany
[d] Steel Institute IEHK, RWTH Aachen University, 52072, Aachen, Germany

ARTICLE INFO

Keywords:
Alloy 400
In situ gas atomization
Laser powder bed fusion
Internal nitridation
TiN nanoparticle
Dispersion strengthening

ABSTRACT

Alloy 400 is a widely used material being known for its excellent corrosive resistance. Within the chemical industry and in contrast to conventional manufacturing processes, Laser Powder Bed Fusion (LPBF) of Alloy 400 opens up for functional components that withstand harsh environments. On the basis of a holistic process route, the present work focusses on modifying the chemical composition of the base material with Titanium in order to allow the formation of TiN nanoparticles during powder production and LPBF, respectively, as well as documenting their influence on the mechanical properties. Parameter optimization for gas atomization and LPBF is carried out and the microstructure of both powders and parts is examined. It was found that besides Cu segregations on grain boundaries and dislocation formation on cell walls, TiN successfully formed in both powders and parts. The Ti-enriched parts resulted in enhanced mechanical properties in terms of hardness, tensile and creep due to these homogeneously distributed dispersoids. Hence, nanoparticle integration proved to be feasible and effective for the present alloy system.

1. Introduction

NiCu-based Alloy 400, also being referred to as Monel 400 or NiCu30Fe, crystalizes in a fcc solid solution and is well known for its excellent corrosion properties [1–3]. Its long-lasting, durable performance in sea water, acids and bases makes it an indispensable alloy system for a wide variety of functional parts in various high-tech industries; in particular, the maritime and chemical sector make frequent use of Alloy 400, utilizing parts such as feedwater and steam generator tubes in power plants, impellers and pump shafts, heat exchangers and condenser tubes in ship building and sour gas resistant components for oil and gas production [4–7]. However, material failure of Alloy 400 at elevated temperatures of 400–800 °C in carbon-rich atmospheres with a low oxygen partial pressure is an issue [8–10]. Conditions like these can be found in syngas power plants, for instance, and lead to metal dusting (MD), a highly detrimental form of corrosion that may fully decompose Ni-based alloys due to extensive coke formation, but by increasing the Cu content this effect can be successfully counteracted [10,11]. Besides MD resistance, creep is significantly determining the lifetime of such components as well and needs to be improved for the present alloy. For instance, for Ni-based SRR99 in the range of 700–900 °C, Yu et al. found that the higher the temperature, the weaker the creep performance [12]. A solution against such rapid creep failure at elevated temperature can be found in the combination of additive manufacturing (AM) and nanoparticle integration [13].

To fabricate near-net-shape, function-integrated parts with little post processing effort, AM shows great potential [14,15]. One of its major benefits is its geometrical freedom, which is given as parts are being manufactured in an iterative process, two-dimensional and layer by layer, resulting in a complete three-dimensional part [16,17]. Thus, AM processes are currently used to produce parts from several alloys such as Ni-based superalloys and steels including stainless steels in various industries [18–24]. Amongst many other AM processes, Laser Powder Bed Fusion is one of the most frequently used ones, in general as well as for Ni-based alloy systems; selective melting of powders results in micro welding of several particles to a consistent part [25,26]. Specimens manufactured by this technique show a completely different microstructure compared to conventional manufacturing processes; they reveal elongated and directed grains with inevitably improved mechanical properties as they are much finer than in castings, for instance

* Corresponding author.
E-mail address: j.roth@hs-osnabrueck.de (J.-P. Roth).

https://doi.org/10.1016/j.msea.2024.146129
Received 22 September 2023; Received in revised form 11 January 2024; Accepted 14 January 2024
Available online 17 January 2024

[27,28]. Also, due to the rapid solidification occurring during LPBF, the phase formation may take place in a non-equilibrium state, which leads to a cellular arrangement of micro dendrites [29–31]. Hence, via the application of LPBF, parts can be tailored to their desired needs, enabling very complex structures not being manufacturable via conventional processes and with an adjusted microstructure.

The study of the integration of nanoparticles into base alloy matrices is becoming more and more intense. Mechanical properties of such reinforced alloy systems, especially in terms of creep and fatigue, outperform unmodified base alloys, also at elevated temperatures [32–35]. The mechanism occurring here is that these nanoscaled dispersoids prevent dislocations from moving throughout the matrix (i.e. dislocation pinning on e.g. oxides) [32,35–39]. Likewise, a positive shift of tensile properties, especially in terms of ultimate tensile strength at high temperatures, can be considered as a further major benefit of nanoparticle integration into base alloys [32,40,41]. Often, the respective nanoparticles can be classified as oxides, which is why the term oxide dispersion strengthening (ODS) was introduced in particular with dispersion strengthening (DS) referring to a wider variety of nanoparticles. Nitrogen can be named as a further frequently used reactive species for DS. In general, there are two different approaches in achieving well dispersed nanoparticles: (i) formation of nanoparticles during LPBF or (ii) implementation of nanoparticles prior to the AM process in terms of modifying the initial base-alloy powder with the respective additives. The first approach makes use of the remaining reactive element (in particular oxygen or nitrogen) within the build chamber of the 3D printer. In the melt pool, prior to solidification, these elements react with further alloying elements showing the lowest free Gibbs energy [32]. Via this routine, Chen et al. successfully integrated well dispersed MnO and Mn_2O_3 in a CoCrFeMnNi high entropy alloy, while Mirzababaei et al. strengthened a FeCrAlY alloy with Y–Al–O and Y–O nanoparticles [42,43]. Hence, nanoscaled dispersoids result throughout the base matrix. Still, in this study, the latter method of altering the feedstock powder was carried out because the build chamber showed a very small remaining number of reactive elements only as it is fully pressured with argon shielding gas. Powders can be modified prior to LPBF by a wide variety of processes such as and amongst others mechanical alloying [33,36,44], acoustic mixing [34], electrostatic assembly techniques [45], electromagnetic three-dimensional vibration [46] or during powder atomization [47–50]. The latter approach was first introduced as gas atomization reaction synthesis (GARS) by Anderson and Foley [50], a procedure, where nanoparticles, such as oxides, eventually form during powder production by introduction of a combination of both reactive and shielding gases [49,51]. DS during atomization comes with several advantages: it is suitable for large-scale production, there is no need for adding nanoparticles as they are formed *in situ* and DS occurs evenly during solidification of the melt to powder. Hence, throughout the present study, this approach of *in situ* atomization was carried out. A pure nitrogen atmosphere was generated within the atomizer as a nano-sized TiN precipitate formation was targeted. The resulting powders were then further processed via LPBF.

2. Experimental procedure

For the atomization of powders, an Indutherm/Blue Power AUG1000HTC atomizer (generator power of 20 kW) was operated with a direct inductive heating capacity in ceramic crucibles up to 1850 °C. Considering appropriate overheating of the system in order to further homogenize the melt and to lower its viscosity, an atomization temperature of 1600 °C was set (liquidus temperature: ~1350 °C). To withstand these high temperatures, ceramic consumables were used – an Al-oxide crucible, stopper rod and outlet (outlet diameter: 2.5 mm). Hot pure nitrogen gas (200 °C) was used for close-coupled atomization and the spray tower was pre-pressured with nitrogen as well. The crucible chamber was pressured with pure argon shielding gas. The gas stream was pressured with 15 bar, adding up in a gas stream of 280 Nm^3/h and a metal mass stream of approx. 4.3 kg/min. The chemical composition of Alloy 400 (approx. 65.0 wt.-% Ni, 31.5 wt.-% Cu, 2.0 wt.-% Fe, 1.0 wt.-% Mn, 0.2 wt.-% Si, 0.2 wt.-% Al, 0.1 wt.-% C) was adjusted in such a way that titanium, which rather can be found in the related Alloy K500 (besides Ti also revealing at least 2.3 wt.-% Al), was added in order to allow for the formation of Ti-nitrides during atomization. Pre-alloyed compounds as well as raw elements were utilized when loading the atomizer crucible with bulk material, resulting in approx. 6.5 kg input per atomization. After atomization, powders were further processed under nitrogen atmosphere, first being sieved and then air-separated by an Indutherm/Blue Power AC1000G air classifier. During this procedure, well processable powder with a desired particle size distribution (PSD) of 15–53 μm was targeted and measured with a Camsizer X2.

After qualifying powders for AM, the LPBF process was initiated, using an EOS AMCM M290 customized machine. Due to its reduced build platform (100 mm in diameter) and pre-heating capability, the equipment allows for the parameter optimization of small batch powder fractions. A green laser system was used under argon atmosphere and a design of experiments (DoE) approach was carried out, varying laser power (p_L) in [W], scanning speed (s_S) in [mm/s] and hatch distance (d_H) in [μm]. The layer thickness (t_L) was at a constant level of 20 μm and the resulting volume energy density (e_V) was defined as per $e_V = p_L/(s_S{*}d_H{*}t_L)$. As an optimum parameter set for the standard Alloy 400, $p_L = 85$ W, $s_S = 1050$ mm/s and $d_H = 50$ μm was found in previous studies [52]. These values served as a basis for the parameter study carried out in this work. Here, at least 99.5 % in optical density was targeted. Mechanical properties of the Ti-enriched Alloy 400 were determined in terms of tensile, creep and hardness testing. For hardness, all values are the average of five separate measurements on five cubes each (25 total measurements for the top as well as for the side surfaces). For the evaluation of optical density and for hardness measurements, cubic samples with an edge length of 8 mm were produced. For density evaluation via light optical microscopy, these were ground down to 2500 grit (SiC paper). For mechanical testing (tensile, creep) instead, a block of 14 × 45 × 70 mm^3 was manufactured and subtractively machined in order to generate the final test specimens. Tensile specimens were generated from M6 x 40 mm cylinders (test area: Ø 3 mm × 9 mm), creep specimens from samples with a 14 × 3.2 mm^2 cross section and total length of 41 mm (test area: 4 × 3.2 mm^2, 25 mm). Stress exponents during creep experiments were obtained as per the formula $\ln(\dot{\varepsilon}) = \ln(B) + n\ln(\sigma^n)$ where $\dot{\varepsilon}$ is the true strain rate, B is a temperature-dependent pre-factor, σ is the applied stress and n is the stress exponent.

In order to investigate powder and part microstructure, a scanning electron microscope (SEM), equipped with energy dispersive X-ray spectroscopy (EDS) as well as electron backscattered diffraction (EBSD), was operated on the microscale. EBSD band contrast (BC) images and crystallographic orientation mappings were both taken with an EBSD Symmetry detector. For more in-depth nanoscale characterization, a transmission electron microscope (TEM) was utilized. Concerning the TEM sample preparation, a thin lamella was extracted from powder particles using a dual beam for focussed Ga^+ ion beam milling (FIB). In order to avoid damage of the area of the future lamella, a very thin platinum layer was deposited using electron deposition and later a thicker platinum layer was applied using ion deposition. This step was followed by gallium ion milling using 30 keV accelerating voltage over a range of currents tuned for precise control over the beam-sample interactions. For rough milling, ion currents of 1–4 nA were applied to produce craters from both sides until a 1.5 μm thick and 10 μm high wall was formed. Subsequently, this pre-lamella was cut free, extracted via a nano-manipulator and welded by platinum to an omniprobe grid. Following milling of the lamella was performed using gentler ion doses, down to electron-transparent thicknesses (<100 nm) with an ion current of 0.1–1 nA. Final polishing was performed with low energy ion milling at 5 KeV and ion current of 250 pA with ±1.5° inclination to the perpendicular direction of the FIB. High-resolution TEM investigations

of lamellae were accomplished by a Talos F200i TEM with FEG electron source in scanning TEM (STEM) mode at 200 kV. To obtain a whole view of the lamellae of powders and additively manufactured parts, the information obtained by bright field (BF) imaging were supplemented by unique EDS absorption correction enabling accurate element quantification. For tensile testing, a universal electromechanical machine was operated, and for creep measurements, a self-designed creep machine developed at the Institute of Physics of Materials as per [53] was used. Vickers-hardness was obtained according to DIN EN ISO 6507-1. Ultimately, mechanical properties were compared to LPBF standard Alloy 400 (without Ti addition) and hot-extruded bulk reference material (also free of Ti), both resulting from previous studies [52].

3. Results and discussion

3.1. Nanoparticle integration into powders

In order to be suitable for LPBF, it is known that as-atomized powders need to be processed. After the removal of splash via sieving at 200 µm, and of particles being either too fine (<15 µm) or too coarse (>53 µm) via air-classification, a particle size distribution that satisfactorily matches the targeted 15–53 µm range was achieved. In Fig. 1, the PSD for the Ti-modified Alloy 400 is displayed in terms of cumulative and relative frequency. It can be clearly seen that the highest yield is between 20 and 25 µm, indicated by the highest column as well as the strongest slope of the line. The particle size at 50 % cumulative frequency amounts to 30.69 µm with 17.26 µm for 10 % and 51.48 µm for 90 %. The yield of powder after air classification within the final PSD was 57 % compared to the crucible input material.

SEM investigations revealed spherical powder particle geometries as shown for a particle of ~55 µm in diameter in Fig. 2. Only negligible satellite formation was observed, further lowering the total surface of a respective particle and thus, enhancing its flowability [54–56]. Spherical particles are generally favorable in AM as they ensure a proper build platform coverage during LPBF. This way, the recoater may supply well flowing powder from the feedstock and consequently build up a homogenous new layer iteratively. Concerning the targeted formation of Ti-nitrides, only little evidence was found at grain boundaries via the application of EDS. As can be seen from the EDS element maps, Ti and N are enriched at the exact same locations in between single grains on the microscale. In contrast, a corresponding proof of the remaining alloying elements forming a chemical bond with nitrogen was not observed. Double-checked via EDS, target values and detected compositions in powders matched. Hence, the preceding atomization process is assumed to operate appropriately; the chemical composition is not affected by any residues or slagging inside the crucible. Also, when printing powders to parts during LPBF, no significant shift in chemistry was detected neither.

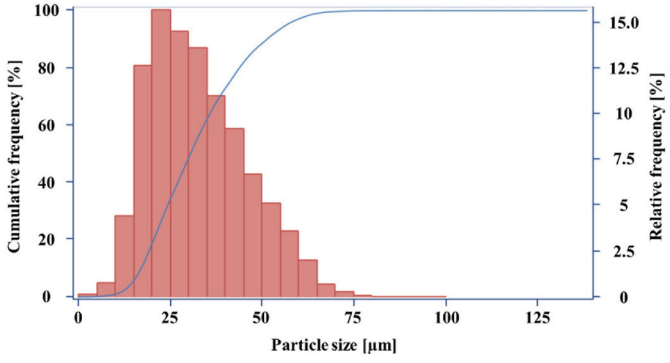

Fig. 1. Particle size distribution in cumulative (blue line) and relative (red columns) frequency. (For interpretation of the references to color in this figure legend, the reader is referred to the Web version of this article.)

In order to indicate an effect on the internal structure of the powder, a lamella was extracted from a single particle and studied by TEM as shown in Fig. 3. Bright and dark field images show dislocation formation along cell walls, resulting from rapid cooling during atomization [57]. Ni and Cu mappings indicate an interdendritic segregation of Cu on cell walls, a well-known characteristic of NiCu alloys [58–60]. Rapid solidification does not allow sufficient Ni diffusion in the dendrites leading to Cu enrichment in the remaining liquid. Besides Cu, no further elements were found to be preferably present on cell walls. Marked by orange arrows, Ti and N enriched areas could be detected near cell walls. They reveal a cuboidal shape corresponding to the characteristic morphology of TiN. Moreover, no further compounds were detected in the same region of interest, leading to the assumption that the targeted TiN formation has successfully been evoked in powders. Accordingly, this reaction has been demonstrated previously for other nanoparticles, such as Y-, Fe- or Cr-oxides, throughout powder production [49,61,62].

3.2. LPBF dispersion-strengthened parts

As the powder was specified as AM-suitable and since noticeable amounts of Ti and N were not dissolved in the matrix but were rather detectable on grain boundaries and cell walls as TiN, these powders were further processed via LPBF in order to achieve TiN formation within the microstructure of the printed parts as well. Even though the LPBF process chamber is pressured with Ar shielding gas, further nitrogen uptake during the manufacturing process might occur as some residual proportions of accompanying gases, such as O or N, inevitably do remain; this was already proven for oxygen uptake in Ar atmosphere for a CoCrFeMnNi alloy and for oxygen uptake in N atmosphere for a FeCrAlY system [42,43]. Hence, the presence of TiN nanoparticles in powders might act as nuclei for an even more pronounced formation of TiN in parts.

Applying a DoE scheme enabled for dense fabrication of the Ti-modified powders into parts. Several parameter sets were evaluated on seventeen cubes as displayed in Table 1. Here, the blue-colored cubes A1 to B2 indicate a variation around the starting point (yellow-colored cubes C3 to C5, initial parameter set found previously for unmodified Alloy 400 [52]) and the orange-colored ones B3 to C2 illustrate extreme points where only one parameter value is shifted. Italic numbers indicate non-varied parameters. Furthermore, the parameter set of cube C2 is highlighted, as it shows the highest attainable optical density throughout this study of 99.84 %. Cross sections of cubes A2, A6, B6 and C2, viewed from the top, are displayed in Fig. 4. Concerning the pore formation within the filling, it can clearly be observed that a too high volume energy density of 169 J/mm^3 for cube A2 leads to the formation of severe defects. The pore size reduces with falling energy density as for A6, pores, resulting from a too high energy input, are still present but they now rather appear as the well-studied key hole defects caused by material evaporation in the melt pool [63,64]. Hence, a decrease of 56 J/mm^3 enables for an increase in density from 97.57 % to 98.65 %. Further lowering the energy density finally allowed the formation of highly dense parts such as B6 (61 J/mm^3 → 99.81 %) or C2 (58 J/mm^3 → 99.84 %). It is important to mention that the missing few per mille to 100 % completely dense parts cannot be correlated with porosities within the filling of the parts but rather have to be located at the edges of the cube as can be seen for all four cross sections. This has been demonstrated by Ertay et al. [65] and Ulbricht et al. [66], assuming that acceleration and deceleration at the end of laser tracks on part edges eventually lead to a localized energy accumulation (which in turn causes key hole porosity). Therefore, in exceeding the targeted 99.5 % in density, C2-parameters (85 W, 1050 mm/s and 70 µm) were considered appropriate and chosen for the further LPBF fabrication of test specimens.

After having found a parameter set for dense part fabrication, SEM and TEM characterizations were carried out. Fig. 5 shows the EBSD BC image in build direction (BD) on the left side and the crystallographic

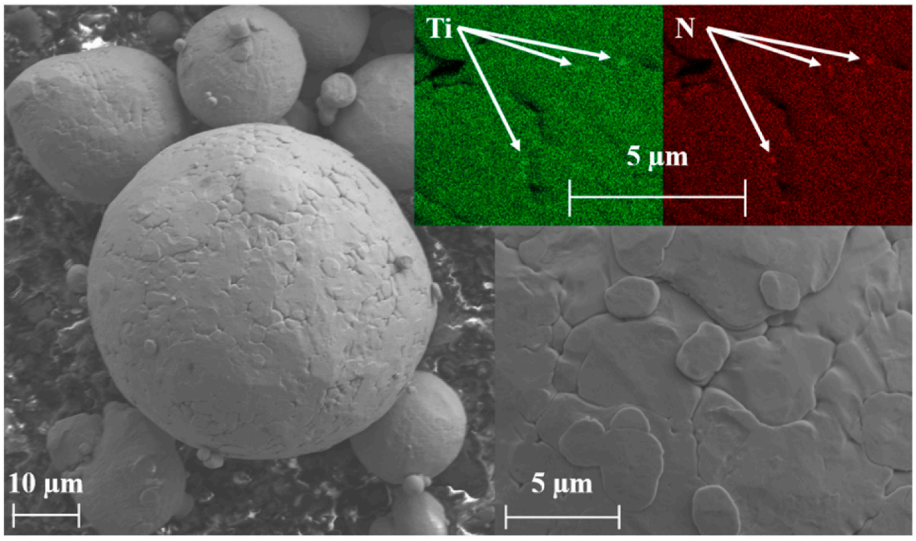

Fig. 2. Ti-enriched particle in the SEM – complete particle with satellites, particle surface and Ti-/N-EDS-mappings.

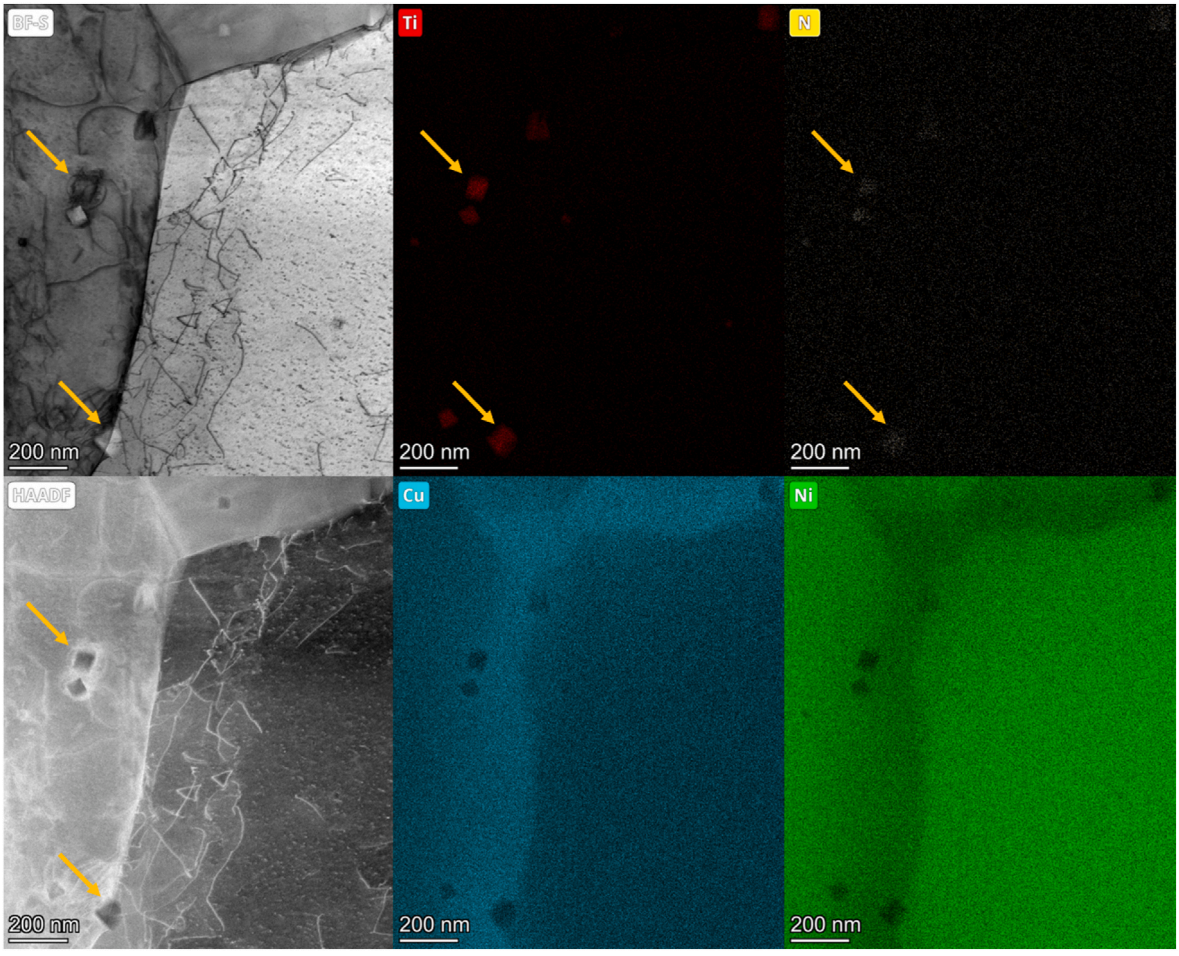

Fig. 3. Bright field, dark field, Ti-, N-, Cu- and Ni-mappings within the modified Alloy 400 powder.

orientation mapping along BD on the right side. The BC image allows for a clear distinguishability between several laser tracks within one respective layer of the part. As mentioned above, 70 µm hatch distance was chosen, resulting in a scan track width of approx. 58 µm. The resulting margin of 12 µm did not result in a lack of fusion between scan tracks due to the iterative sequence of several part layers, all being exposed in another orientation around the BD-axis and leading to the formation of a heat-affected zone as commonly known for LPBF [67,68]. This way, porosity eventually gets prevented as sufficient energy and material are applied to one respective layer. The EBSD image was taken from another perspective, illustrating the grain growth along the build direction when viewed from the side. A well-studied peculiarity of AM is

Table 1
Parameter sets for different cubes, resulting in volume energy densities and optical relative densities, respectively.

Cube	Laser power in [W]	Scanning speed in [mm/s]	Hatch distance in [µm]	Volume energy density in [J/mm³]	Optical relative density in [%]
A1	55	850	40	81	95.18
A2	115	850	40	169	97.57
A3	55	1250	40	55	95.29
A4	115	1250	40	115	96.93
A5	55	850	60	54	98.70
A6	115	850	60	113	98.65
B1	55	1250	60	37	95.14
B2	115	1250	60	77	98.33
B3	35	*1050*	*50*	33	90.41
B4	136	*1050*	*50*	129	98.75
B5	*85*	714	*50*	119	97.47
B6	*85*	1386	*50*	61	99.81
C1	*85*	*1050*	30	135	98.51
C2	***85***	***1050***	**70**	**58**	**99.84**
C3	*85*	*1050*	*50*	81	99.64
C4	*85*	*1050*	*50*	81	99.80
C5	*85*	*1050*	*50*	81	99.57

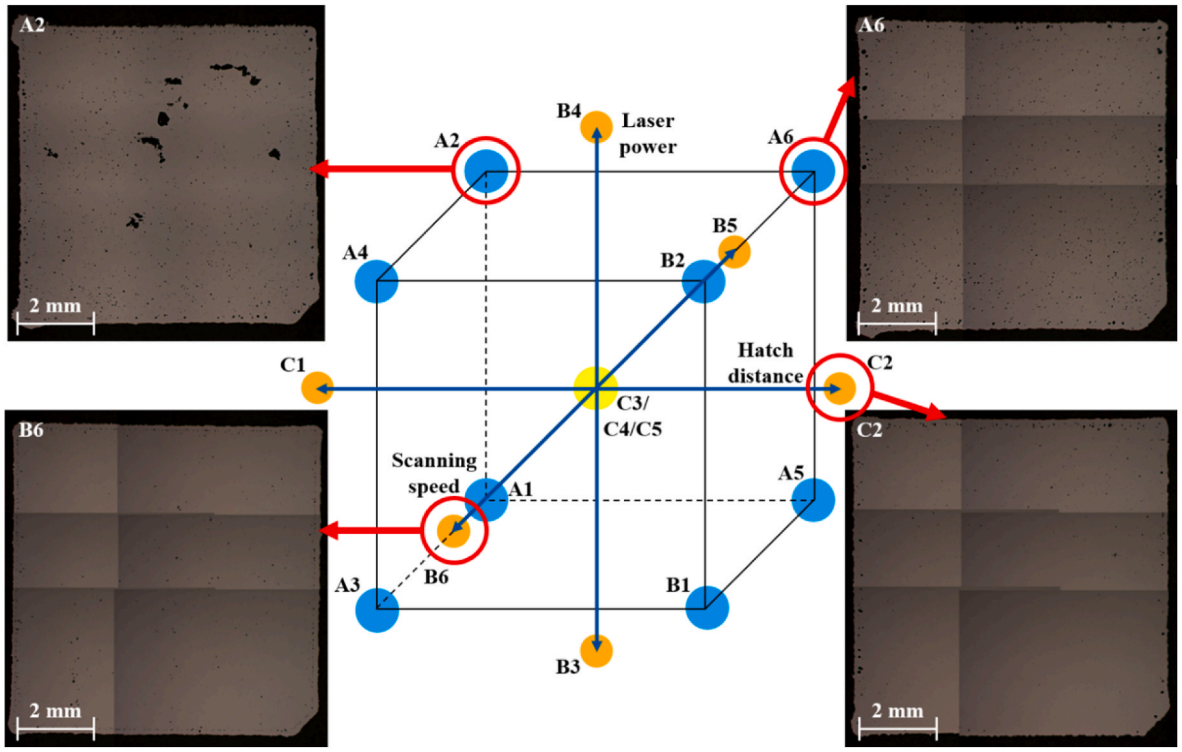

Fig. 4. Design of experiments cube, revealing the location of the above-mentioned parameter sets within the design space, and corresponding cross sections of cubes A2, A6, B6 and C2.

that grains show a clear tendency in growing along BD, being correlated with both the direction of energy input and the heat flow [69,70]. Regarding the respective fcc crystal structure, a wide variety of preferred orientations was detected. As indicated by the inverse pole figure, no preferred texture was verified with respect to the BD. Qin et al. showed a weakly pronounced texture for LPBF-AlSiMg as well and justified it with the rotating scanning strategy (which amounted to 67° as in this work) [68]. As layers get re-melted several times and in varying orientations, no preference in orientation can evolve.

The Ti and N enrichments found in the powder were expected to reappear in the parts. So, TEM characterization was carried out to study the microstructure on the nanoscale. Fig. 6 illustrates the respective findings. Having a look at the dark and bright field images in the first row, a cellular structure becomes clearly visible. The micro-dendritic

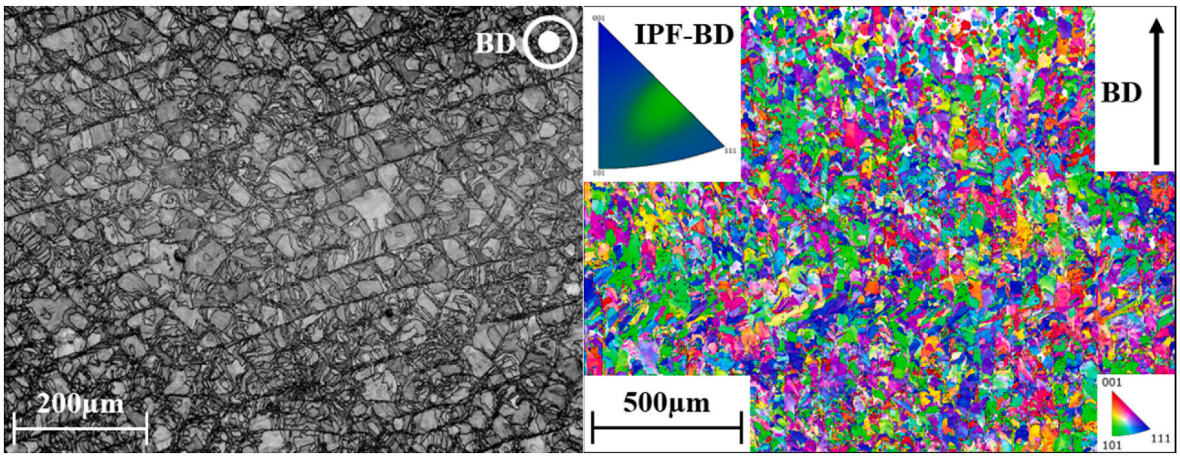

Fig. 5. EBSD band contrast for the top-down view in BD (left) and EBSD map for the side view along BD (right).

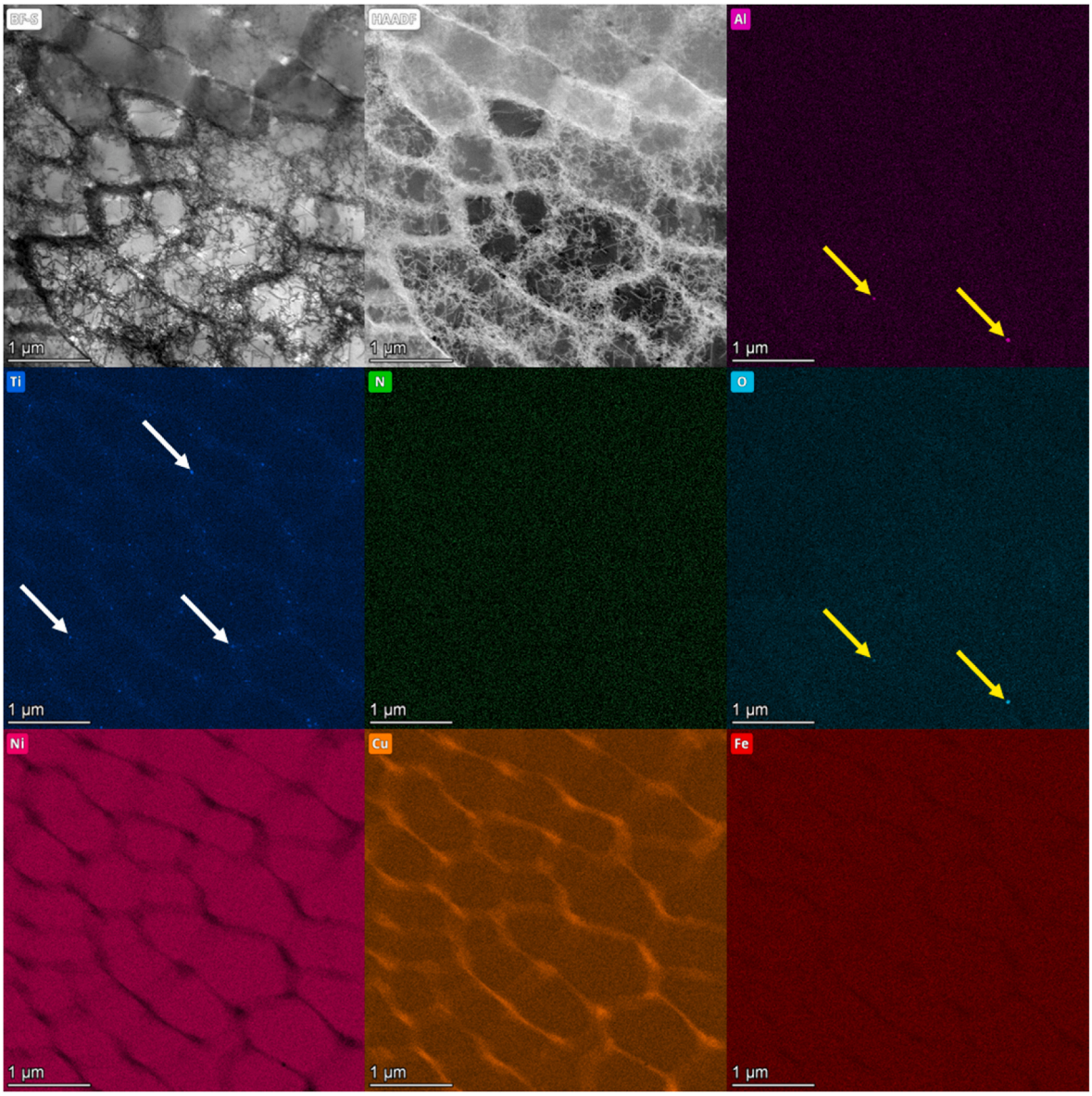

Fig. 6. Bright field, dark field, Al-, Ti-, N-, O-, Ni-, Cu-, and Fe-mappings within the modified Alloy 400 part, Ti highlighted with white arrows, Al and O highlighted with yellow arrows. (For interpretation of the references to color in this figure legend, the reader is referred to the Web version of this article.)

cell walls are comprised of a high number of dislocations, while cell cores experience a weaker intensity in dislocations. This is due to the fact that segregations at cell walls of solid solutions facilitate the nucleation of dislocations [71]. Also, compared to the powder lamella in Fig. 3, the dislocation density is significantly higher. High dislocation density and micro dendritic structures within single grains, resulting from the occurring high cooling rates, are frequently investigated phenomena in AM for a wide variety of alloys and thus, they were expected and also verified for the present alloy system as well [52,72–75]. Having a closer look at these cell walls dense in dislocations, nano-segregations can be detected for Cu and, in lower intensity, for Ti. In contrast, Ni and Fe are rather present within the cells than at their boundaries. As found in powders already, such Cu segregations are a common property of NiCu-based alloys that have been reported intensively for decades [58–60]; they are due to the insufficient interdiffusion within the solid nuclei in the two-phase regime, leading to an interdendritic Cu enrichment. For Ti, a high number of nano-scaled precipitates can be reported on cell walls, some of them being marked with white arrows. However, via application of this characterization technique, no such precipitates could be verified for N by STEM-EDS which is due to the limited quantifiability by this technique. Fig. 7 reveals the presence of precipitates in higher resolution, probably being TiN. The cuboidal nanoparticles can be clearly detected on the cell walls within single grains, and its morphology is typical for the occurrence of TiN. This characteristic shape has been reported frequently in literature already [76–79]. The formation mechanism can be traced back to a low standard free energy of TiN. The presence of Ti and N outside the preferred solid solution was targeted throughout this work and is now expected to have an influence on the mechanical properties in comparison to Alloy 400 without any Ti addition.

Besides this finding, the occasional presence of Al and O was detected and indicated by yellow arrows. Hence, Al-oxide seems to form as a secondary by-product in marginal quantity. As stated by Xu et al. and Hadraba et al. for Y-oxides, this may eventually lead to the pinning of dislocations [32,36]. Still, with the present alloy and its very low pronounced Al-oxide formation, it cannot be assumed that these nanoparticles will cause any effect on the mechanical properties; mechanical improvements can only be associated with the TiN formation.

3.3. Enhanced mechanical properties

As the formation of TiN (and to a significantly lesser extent of Al_2O_3) seems to take place during LPBF, mechanical properties are expected to outperform the ones of non-modified Alloy 400. The latter key figures were elaborated in previous work [52] already. For hardness according to Vickers, HV10 was specified as listed in Table 2 and measured on as-built surfaces. While the Ti-enriched Alloy 400 shows a high hardness on the top surface, which exceeds the non-modified standard version of the alloy by approx. 15 HV10, the side surfaces reveal a lower hardness which in turn is approx. 15 HV10 below the reference value. This finding can be correlated to the pronounced pore formation below the side surfaces of the parts, as illustrated in Fig. 4 already, which occurred to a lesser extent in the reference material. During hardness measurements, such voids facilitate the penetration of the Vickers geometry. Therefore, the mean value of 207.4 HV10 of the top surface, where no such pore formation was observed, better indicates the hardness potential of the present modified alloy, outperforming the unmodified version. In conventionally manufactured, hot-extruded bulk material, only 121–127 HV10 can be reached [52]. This can be explained by the overall finer grain structure of the LPBF-manufactured parts, as discussed by Raffeis et al. for a NiCu-based alloy [3]. To summarize, a clear hierarchy can be noted: Ti-enriched Alloy 400 shows a higher hardness than unmodified Alloy 400 which in turn demonstrates a higher hardness than conventionally manufactured bulk material. An increase in hardness due to DS is a well-studied characteristic throughout literature; for instance, Elsayed et al. denoted a 20 % increase in Vickers hardness after modifying an AlSi10Mg with B_4C and Gao et al. reached a 16 % increase due to TiN integration into the same base alloy [46,80].

Fig. 8 illustrates the results of tensile tests for (i) the Ti-enriched Alloy 400 ('LPBF + Ti'), (ii) hot-extruded bulk Alloy 400 ('bulk'), taken from previous work [52], and (iii) the standard LPBF version of

Table 2
Hardness for Ti-enriched and unmodified LPBF Alloy 400.

Hardness	HV10
Ti-enriched	207.4 ± 4.2 (top surface)
Alloy 400	179.8 ± 5.4 (side surface)
Standard	192.9 ± 3.1 (top surface)
Alloy 400	194.9 ± 3.2 (side surface)

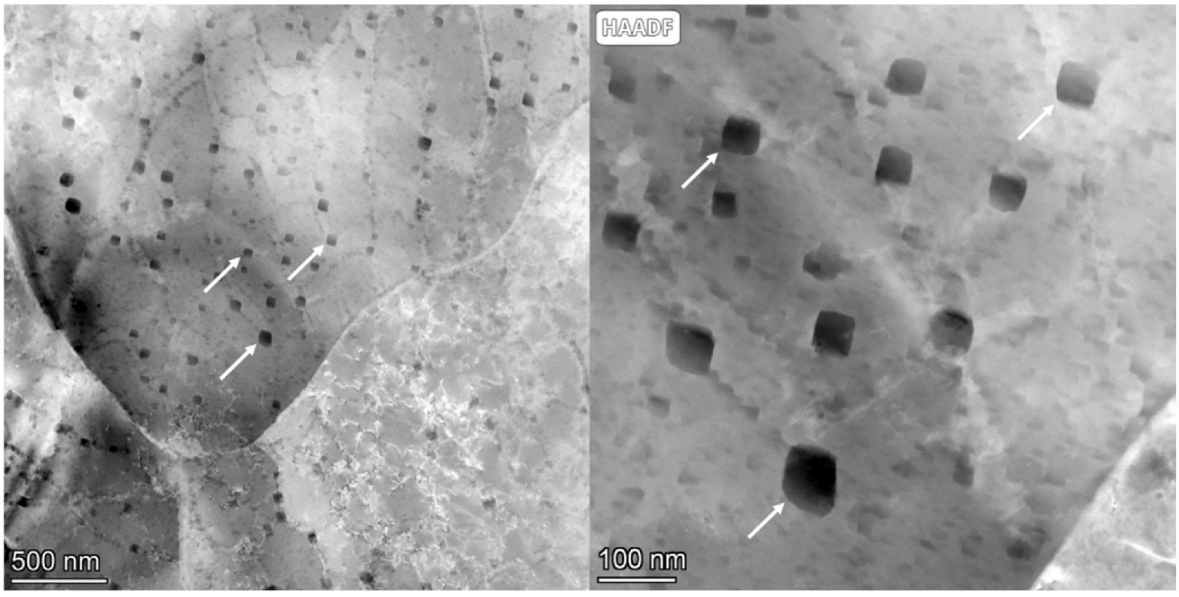

Fig. 7. Dark-field TEM of cuboidal TiN nanoparticles on sub-grain cell walls.

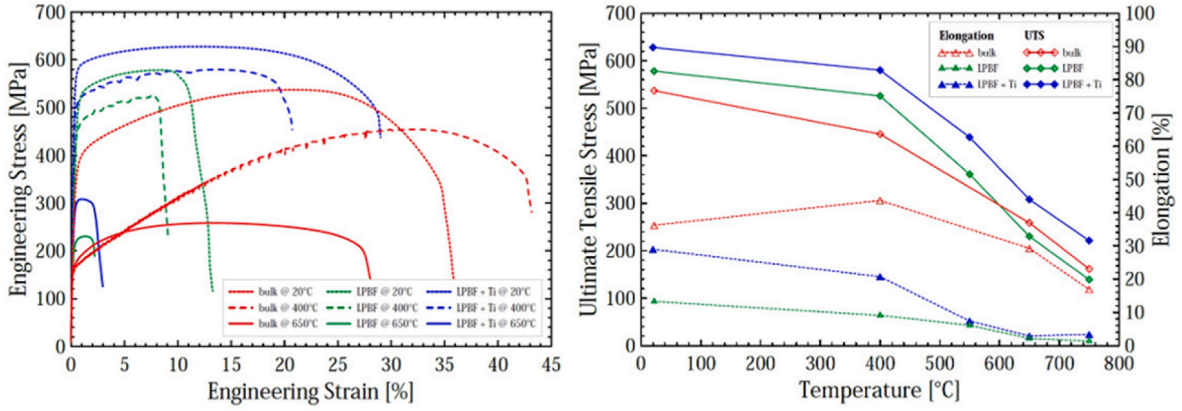

Fig. 8. Stress-strain curves at several temperatures and UTS & elongation over temperature for the three variants of Alloy 400.

Alloy 400 containing no Ti ('LPBF'). When comparing the tensile curves for the three different material types at temperatures of 20 °C, 400 °C and 650 °C (potential application temperatures of Alloy 400 heat exchangers), they all show the highest attainable stress for room temperature and lowest for 650 °C, respectively. Also, the Ti-enriched Alloy 400 shows higher strength levels for all temperatures than the other two versions (with 'LPBF' being slightly higher or equal to 'bulk'). Higher strength is attributed to the finer grain size of the AM variants [3,27,28]. Moreover, TiN particles on cell boundaries seem to positively affect the ultimate tensile strength (UTS) of 'LPBF + Ti' even further as it lies at least ~ 50 MPa above the 'LPBF' values for all tested temperatures (20 °C, 400 °C, 550 °C, 650 °C and 750 °C). When comparing the strains at fracture (elongations) as a measure of ductility, the bulk variant outperforms both LPBF variants throughout the whole temperature range. The remaining porosity and the high dislocation densities at the cell boundaries in the LPBF versions serve as an explanation here. The 'LPBF + Ti' version reveals better strain performance than the 'LPBF' variant. However, this effect becomes negligible at temperatures ≥550 °C. At room temperature, the strain of the Ti-modified LPBF version almost reaches bulk performance. An overall positive effect of the TiN nano precipitates can be noted at this stage; especially contributing to a better strength performance. Improved tensile properties due to DS are a well-studied phenomenon. Yu et al. correlated an increase in tensile strength for a Ni-based superalloy with the presence of several oxides on the nanoscale [40]. Accordingly, Jang et al. reported that ODS Ni-based alloys outperform the non-modified versions in terms of mechanical properties at elevated temperatures due to suppression of dislocation movement; e.g. a 84 % increase at 700 °C for alloy 617 was reported [41]. For a NiCrFeY alloy enriched with Y_2O_3, Xu et al. revealed a high ultimate tensile strength around 563 MPa at 600 °C, traced back to the interplay of a high dislocation density and the nanoparticles [32].

Shifting the focus to the targeted enhanced creep properties due to TiN-precipitate-induced dislocation pinning, Fig. 9 shows the test results for 'LPBF + Ti', 'bulk' and 'LPBF'. The image on the left-hand side illustrates the correlation between the applied stress σ in [MPa] and the time to fracture t_f in [h]. At approx. 50, 80 and 100 MPa, a comparison between the three different alloy states is most accurate as measuring points are available for all of them. From the measured time to fracture data at various stress levels, it can be concluded that the creep properties of bulk material and Ti-enhanced LPBF material outperform the unmodified alloy, while the bulk one shows slightly higher values than 'LPBF + Ti'. It may thus be concluded that the AM variants of Alloy 400 do not show better creep performance than the conventionally fabricated material. However, comparing only the two LPBF variants, a clear shift in terms of enhanced creep properties can be attributed to the Ti-alloyed material. Therefore, the previously found TiN nanoparticles on cell walls seem to have a certain impact on dislocation pinning. Al-oxides might also slightly contribute here but occur considerably less in the nanostructure than the Ti-nitrides. Fig. 9 right illustrates the detected stress exponent n for the respective material types 'bulk', 'LPBF' and 'LPBF + Ti', resulting from the applied stress levels σ in [MPa] and steady creep rates $\dot{\varepsilon}$ in [%/s] at 650 °C (determined at a strain of ε = 1 %). Accordingly, the stress exponents are: n = 3.1 for 'LPBF, n = 4.9 for 'bulk' and n = 4.8 for 'LPBF + Ti'. Therefore, the bulk and the Ti-enhanced LPBF variants can be described as significantly more resistant to creep with stress exponents of an order around n = 5 (which corresponds to a typical value for pure metals); the unmodified LPBF version instead reveals a stress exponent around n = 3, matching the typical order for solid solutions [81]. Also, when comparing the data for 100 MPa applied stress, the steady creep rate for the standard LPBF Alloy 400

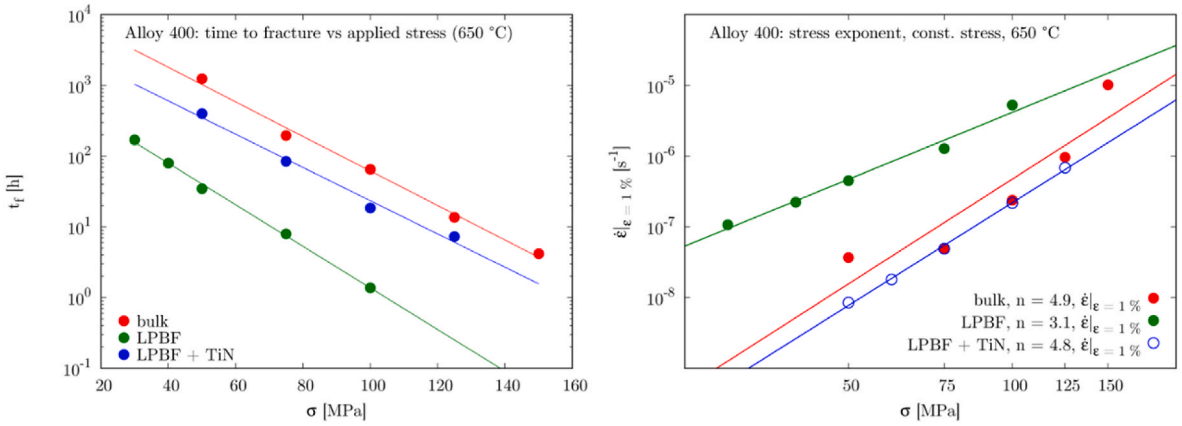

Fig. 9. Time to fracture and stress exponents, resulting from creep experiments at 650 °C for the three variants of Alloy 400.

measures approx. 10^{-5}/s, while the other two reveal a rate of ~10^{-7}/s. Hence, creep takes place more slowly, allowing to conclude for a positive effect on the creep properties due to TiN, enabling for comparable creep properties as in bulk material. For several Fe-based, ferritic alloys, Wasilkowska et al. exemplified that, especially at elevated temperatures, there is a clear positive effect of ODS nanoparticles on creep performance, being correlated with a successful pinning of dislocations [37]. The same finding of a positive ODS-dislocation-creep connection at 950 °C was found by Rakhmonov et al. for Hastelloy X reinforced by Y_2O_3 [38]. For a gas-nitrided AISI 316L steel, Boes et al. stated that both nitrides and carbonitrides, e.g. enriched in Ti, inevitably improve the creep performance of the alloy [39].

4. Conclusion

In this work, a nanoparticle modification route for a Ti-enriched, NiCu-based Alloy 400 was established. The process consisted of the nitrogen atomization of raw material to powder being suitable for AM, a DoE-assisted LPBF parameter optimization for manufacturing of highly dense parts and a determination of mechanical properties in terms of hardness, tensile and creep. In between, an in-depth characterization of powders and parts was carried out. It was aimed to introduce TiN particles on the sub-grain nanoscale. Enrichments of Ti and N were detected on powder surfaces and TiN was proven to be present inside powders, resulting from the internal nitridation during atomization. TiN formation was determined on cell walls of the LPBF built parts as well. This eventually led to enhanced mechanical properties, resulting from the Ti modification of the standard Alloy 400 and the respective TiN nanoparticles. The proven improvements include:

- A positive shift in Vickers hardness of 15 HV10 to 207 HV10 in total for the Ti-enriched variant when compared to the unmodified LPBF one.
- Enhanced ultimate tensile strength of the Ti-enhanced version throughout the whole tested temperature range (room temperature up to 750 °C) when compared to bulk material and non-modified LPBF Alloy 400.
- A comparably high elongation for 'LPBF + Ti' and 'bulk' at 20 °C, while for all temperatures above the strain rates of the bulk material are substantially higher than the ones of the LPBF versions.
- Comparable creep performance of the LPBF variant including Ti to the bulk one, both being clearly higher than for the standard LPBF Alloy 400 by one order of magnitude, allowing for a substantially longer time to fracture for several applied stresses.

To conclude, a nanoparticle modification is feasible for the present Alloy 400 system enriched in Ti as TiN formed *in situ* during nitrogen atomization and in the subsequent LPBF process. This, in turn, successfully limited dislocation movement on the nanoscale and allowed for superior mechanical properties when compared to the unmodified version of the alloy system.

CRediT authorship contribution statement

J.-P. Roth: Conceptualization, Data curation, Formal analysis, Investigation, Methodology, Software, Supervision, Validation, Visualization, Writing – original draft, Writing – review & editing. **I. Šulák:** Data curation, Investigation, Software, Visualization, Writing – review & editing. **Z. Chlup:** Data curation, Investigation, Software, Visualization, Writing – review & editing. **J. Fischer-Bühner:** Investigation, Writing – review & editing. **U. Krupp:** Conceptualization, Funding acquisition, Project administration, Resources, Supervision, Writing – review & editing. **K. Jahns:** Conceptualization, Funding acquisition, Project administration, Resources, Supervision, Writing – review & editing.

Declaration of competing interest

The authors declare that they have no known competing financial interests or personal relationships that could have appeared to influence the work reported in this paper.

Data availability

Data will be made available on request.

Acknowledgements

The authors would like to acknowledge QuesTek Europe AB for providing the Ti-modified alloy composition. This work has received funding from the European Union's Horizon 2020 research and innovation program under grant agreement No 958192 which is gratefully acknowledged.

References

[1] Special Metals Corporation, Monel alloy 400 (2005).
[2] C.-H. Zhang, C.-L. Wu, S. Zhang, Y.-F. Jia, M. Guan, J.-Z. Tan, B. Lin, Laser cladding of NiCrSiB on Monel 400 to enhance cavitation erosion and corrosion resistance, Rare Met. 41 (2022) 4257–4265, https://doi.org/10.1007/s12598-016-0814-4.
[3] I. Raffeis, F. Adjei-Kyeremeh, U. Vroomen, E. Westhoff, S. Bremen, A. Hohoi, A. Bührig-Polaczek, Qualification of a Ni–Cu alloy for the laser powder bed fusion process (LPBF): its microstructure and mechanical properties, Appl. Sci. 10 (2020) 3401, https://doi.org/10.3390/app10103401.
[4] R.K. Devendranath, N. Arivazhagan, S. Narayanan, M. Narayanan, A. Mondody, R. Kashyap, Development of defect free monel 400 welds for marine application, AMR 383–390 (2011) 4693–4696, https://doi.org/10.4028/www.scientific.net/AMR.383-390.4693.
[5] U. Esgin, D. Özyürek, H. Kaya, An investigation of wear behaviors of different Monel alloys produced by powder metallurgy, AIP Conf. Proc. 1727 (2016) 20008, https://doi.org/10.1063/1.4945963.
[6] L.E. Shoemaker, G.D. Smith, A century of monel metal: 1906–2006, JOM 58 (2006) 22–26, https://doi.org/10.1007/s11837-006-0077-x.
[7] Special Metals Corporation, High-Performance Alloys for Resistance to Aqueous Corrosion, 2000.
[8] D.J. Young, J. Zhang, C. Geers, M. Schütze, Recent advances in understanding metal dusting: a review, Mater. Corros. 62 (2011) 7–28, https://doi.org/10.1002/maco.201005675.
[9] R. Schneider, E. Pippel, J. Woltersdorf, S. Strauß, H.J. Grabke, Microprocesses of metal dusting on nickel and Ni-base alloys, Steel Res. 68 (1997) 326–332, https://doi.org/10.1002/srin.199701796.
[10] K. Jahns, A.S. Ulrich, C. Schlereth, L. Reiff, U. Krupp, M.C. Galetz, The effect of Cu content and surface finish on the metal dusting resistance of additively manufactured NiCu alloys, Oxid Met 96 (2021) 241–256, https://doi.org/10.1007/s11085-021-10037-8.
[11] C. Geers, Inhibition of Coking and Metal Dusting on Conventional Alloys by Using a Nickel-Tin Intermetallic Coating, 2013.
[12] J. Yu, X. Sun, T. Jin, N. Zhao, H. Guan, Z. Hu, High temperature creep and low cycle fatigue of a nickel-base superalloy, Mater. Sci. Eng., A 527 (2010) 2379–2389, https://doi.org/10.1016/j.msea.2010.01.001.
[13] C. Doñate-Buendía, F. Frömel, M.B. Wilms, R. Streubel, J. Tenkamp, T. Hupfeld, M. Nachev, E. Gökce, A. Weisheit, S. Barcikowski, F. Walther, J.H. Schleifenbaum, B. Gökce, Oxide dispersion-strengthened alloys generated by laser metal deposition of laser-generated nanoparticle-metal powder composites, Mater. Des. 154 (2018) 360–369, https://doi.org/10.1016/j.matdes.2018.05.044.
[14] O. Abdulhameed, A. Al-Ahmari, W. Ameen, S.H. Mian, Additive manufacturing: challenges, trends, and applications, Adv. Mech. Eng. 11 (2019) 168781401882288, https://doi.org/10.1177/1687814018822880.
[15] B. Cox, M. Ghayoor, R.P. Doyle, S. Pasebani, J. Gess, Numerical model of heat transfer during laser powder bed fusion of 316L stainless steel, Int. J. Adv. Manuf. Technol. 119 (2022) 5715–5725, https://doi.org/10.1007/s00170-021-08352-0.
[16] C. Klahn, B. Leutenecker, M. Meboldt, Design for additive manufacturing – supporting the substitution of components in series products, Procedia CIRP 21 (2014) 138–143, https://doi.org/10.1016/j.procir.2014.03.145.
[17] A. Hussein, L. Hao, C. Yan, R. Everson, P. Young, Advanced lattice support structures for metal additive manufacturing, J. Mater. Process. Technol. 213 (2013) 1019–1026, https://doi.org/10.1016/j.jmatprotec.2013.01.020.
[18] G. Çam, Prospects of producing aluminum parts by wire arc additive manufacturing (WAAM), Mater. Today: Proc. 62 (2022) 77–85, https://doi.org/10.1016/j.matpr.2022.02.137.
[19] Ö.S. Bölükbaşı, T. Serindağ, U. Gürol, A. Günen, G. Çam, Improving oxidation resistance of wire arc additive manufactured Inconel 625 Ni-based superalloy by pack aluminizing, CIRP Journal of Manufacturing Science and Technology 46 (2023) 89–97, https://doi.org/10.1016/j.cirpj.2023.07.011.
[20] U. Gürol, Y. Altınay, A. Günen, Ö.S. Bölükbaşı, M. Koçak, G. Çam, Effect of powder-pack aluminizing on microstructure and oxidation resistance of wire arc additively

manufactured stainless steels, Surf. Coating. Technol. 468 (2023) 129742, https://doi.org/10.1016/j.surfcoat.2023.129742.
[21] A. Günen, U. Gürol, M. Koçak, G. Çam, A new approach to improve some properties of wire arc additively manufactured stainless steel components: simultaneous homogenization and boriding, Surf. Coating. Technol. 460 (2023) 129395, https://doi.org/10.1016/j.surfcoat.2023.129395.
[22] A. Günen, U. Gürol, M. Koçak, G. Çam, Investigation into the influence of boronizing on the wear behavior of additively manufactured Inconel 625 alloy at elevated temperature, Prog Addit Manuf 8 (2023) 1281–1301, https://doi.org/10.1007/s40964-023-00398-8.
[23] F. Ceritbinmez, A. Günen, U. Gürol, G. Çam, A comparative study on drillability of Inconel 625 alloy fabricated by wire arc additive manufacturing, J. Manuf. Process. 89 (2023) 150–169, https://doi.org/10.1016/j.jmapro.2023.01.072.
[24] N. Zhao, M. Parthasarathy, S. Patil, D. Coates, K. Myers, H. Zhu, W. Li, Direct additive manufacturing of metal parts for automotive applications, J. Manuf. Syst. 68 (2023) 368–375, https://doi.org/10.1016/j.jmsy.2023.04.008.
[25] Z. Tian, C. Zhang, D. Wang, W. Liu, X. Fang, D. Wellmann, Y. Zhao, Y. Tian, A review on laser powder bed fusion of inconel 625 nickel-based alloy, Appl. Sci. 10 (2020) 81, https://doi.org/10.3390/app10010081.
[26] S. Sanchez, P. Smith, Z. Xu, G. Gaspard, C.J. Hyde, W.W. Wits, I.A. Ashcroft, H. Chen, A.T. Clare, Powder Bed Fusion of nickel-based superalloys: a review, Int. J. Mach. Tool Manufact. 165 (2021) 103729, https://doi.org/10.1016/j.ijmachtools.2021.103729.
[27] M. Avateffazeli, P.E. Carrion, B. Shachi-Amirkhiz, H. Pirgazi, M. Mohammadi, N. Shamsaei, M. Haghshenas, Correlation between tensile properties, microstructure, and processing routes of an Al–Cu–Mg–Ag–TiB2 (A205) alloy: additive manufacturing and casting, Mater. Sci. Eng., A 841 (2022) 142989, https://doi.org/10.1016/j.msea.2022.142989.
[28] P. Krakhmalev, G. Fredriksson, K. Svensson, I. Yadroitsev, I. Yadroitsava, M. Thuvander, R. Peng, Microstructure, solidification texture, and thermal stability of 316 L stainless steel manufactured by laser powder bed fusion, Metals 8 (2018) 643, https://doi.org/10.3390/met8080643.
[29] W. Abd-Elaziem, S. Elkatatny, A.-E. Abd-Elaziem, M. Khedr, M.A. Abd El-baky, M. A. Hassan, M. Abu-Okail, M. Mohammed, A. Järvenpää, T. Allam, A. Hamada, On the current research progress of metallic materials fabricated by laser powder bed fusion process: a review, J. Mater. Res. Technol. 20 (2022) 681–707, https://doi.org/10.1016/j.jmrt.2022.07.085.
[30] J.J. Lewandowski, M. Seifi, Metal additive manufacturing: a review of mechanical properties, Annu. Rev. Mater. Res. 46 (2016) 151–186, https://doi.org/10.1146/annurev-matsci-070115-032024.
[31] L. Thijs, K. Kempen, J.-P. Kruth, J. van Humbeeck, Fine-structured aluminium products with controllable texture by selective laser melting of pre-alloyed AlSi10Mg powder, Acta Mater. 61 (2013) 1809–1819, https://doi.org/10.1016/j.actamat.2012.11.052.
[32] R. Xu, Z. Geng, Y. Wu, C. Chen, M. Ni, D. Li, T. Zhang, H. Huang, F. Liu, R. Li, K. Zhou, Microstructure and mechanical properties of in-situ oxide-dispersion-strengthened NiCrFeY alloy produced by laser powder bed fusion, Advanced Powder Materials 1 (2022) 100056, https://doi.org/10.1016/j.apmate.2022.100056.
[33] T.M. Smith, C.A. Kantzos, N.A. Zarkevich, B.J. Harder, M. Heczko, P.R. Gradl, A. C. Thompson, M.J. Mills, T.P. Gabb, J.W. Lawson, A 3D printable alloy designed for extreme environments, Nature 617 (2023) 513–518, https://doi.org/10.1038/s41586-023-05893-0.
[34] T.M. Smith, A.C. Thompson, T.P. Gabb, C.L. Bowman, C.A. Kantzos, Efficient production of a high-performance dispersion strengthened, multi-principal element alloy, Sci. Rep. 10 (2020) 9663, https://doi.org/10.1038/s41598-020-66436-5.
[35] J.H. Martin, B.D. Yahata, J.M. Hundley, J.A. Mayer, T.A. Schaedler, T.M. Pollock, 3D printing of high-strength aluminium alloys, Nature 549 (2017) 365–369, https://doi.org/10.1038/nature23894.
[36] H. Hadraba, Z. Chlup, A. Dlouhy, F. Dobes, P. Roupcova, M. Vilemova, J. Matejicek, Oxide dispersion strengthened CoCrFeNiMn high-entropy alloy, Mater. Sci. Eng., A 689 (2017) 252–256, https://doi.org/10.1016/j.msea.2017.02.068.
[37] A. Wasilkowska, M. Bartsch, U. Messerschmidt, R. Herzog, A. Czyrska-Filemonowicz, Creep mechanisms of ferritic oxide dispersion strengthened alloys, J. Mater. Process. Technol. 133 (2003) 218–224, https://doi.org/10.1016/S0924-0136(02)00237-6.
[38] J.U. Rakhmonov, C. Kenel, A. de Luca, C. Leinenbach, D.C. Dunand, Effect of Y2O3 dispersoids on microstructure and creep properties of Hastelloy X processed by laser powder-bed fusion, Additive Manufacturing Letters 3 (2022) 100069, https://doi.org/10.1016/j.addlet.2022.100069.
[39] J. Boes, A. Röttger, L. Becker, W. Theisen, Processing of gas-nitrided AISI 316L steel powder by laser powder bed fusion – microstructure and properties, Addit. Manuf. 30 (2019) 100836, https://doi.org/10.1016/j.addma.2019.100836.
[40] L. Yu, Z. Lu, J. Xian, X. Chen, S. Peng, X. Li, H. Li, Effects of Al content on microstructure and tensile properties of Ni-based ODS superalloys, J. Alloys Compd. 941 (2023) 168965, https://doi.org/10.1016/j.jallcom.2023.168965.
[41] J. Jang, T.K. Kim, C.H. Han, H.-K. Min, S.-H. Jeong, D.H. Kim, A preliminary development and characterization of Ni-based ODS alloys, Procedia Eng. 55 (2013) 284–288, https://doi.org/10.1016/j.proeng.2013.03.255.
[42] P. Chen, C. Yang, S. Li, M.M. Attallah, M. Yan, In-situ alloyed, oxide-dispersion-strengthened CoCrFeMnNi high entropy alloy fabricated via laser powder bed fusion, Mater. Des. 194 (2020) 108966, https://doi.org/10.1016/j.matdes.2020.108966.
[43] S. Mirzababaei, M. Ghayoor, R.P. Doyle, S. Pasebani, In-situ manufacturing of ODS FeCrAlY alloy via laser powder bed fusion, Mater. Lett. 284 (2021) 129046, https://doi.org/10.1016/j.matlet.2020.129046.
[44] M. Li, Y. Guo, W. Li, Y. Zhang, Y. Chang, Property enhancement of CoCrNi medium-entropy alloy by introducing nano-scale features, Mater. Sci. Eng., A 817 (2021) 141368, https://doi.org/10.1016/j.msea.2021.141368.
[45] J.H. Martin, B.D. Yahata, J.M. Hundley, J.A. Mayer, T.A. Schaedler, T.M. Pollock, 3D printing of high-strength aluminium alloys, Nature 549 (2017) 365–369, https://doi.org/10.1038/nature23894.
[46] A. Elsayed, C. Haase, U. Krupp, Additive manufacturing of metal matrix nanocomposites: novel approach for nanoparticles dispersion by electromagnetic three-dimensional vibration, Mater. Lett. 344 (2023) 134399, https://doi.org/10.1016/j.matlet.2023.134399.
[47] T. Horn, C. Rock, D. Kaoumi, I. Anderson, E. White, T. Prost, J. Rieken, S. Saptarshi, R. Schoell, M. DeJong, S. Timmins, J. Forrester, S. Lapidus, R. Napolitano, D. Zhang, J. Darsell, Laser powder bed fusion additive manufacturing of oxide dispersion strengthened steel using gas atomized reaction synthesis powder, Mater. Des. 216 (2022) 110574, https://doi.org/10.1016/j.matdes.2022.110574.
[48] S. Saptarshi, M. deJong, C. Rock, I. Anderson, R. Napolitano, J. Forrester, S. Lapidus, D. Kaoumi, T. Horn, Laser powder bed fusion of ODS 14YWT from gas atomization reaction synthesis precursor powders, JOM 74 (2022) 3303–3315, https://doi.org/10.1007/s11837-022-05418-6.
[49] D. Zhang, J.T. Darsell, J. Wang, X. Ma, G.J. Grant, I.E. Anderson, J.R. Rieken, D. J. Edwards, W. Setyawan, T.J. Horn, G.R. Odette, No ball milling needed: alternative ODS steel manufacturing with gas atomization reaction synthesis (GARS) and friction-based processing, J. Nucl. Mater. 566 (2022) 153768, https://doi.org/10.1016/j.jnucmat.2022.153768.
[50] I.E. Anderson, J.C. Foley, Determining the role of surfaces and interfaces in the powder metallurgy processing of aluminum alloy powders, Surf. Interface Anal. 31 (2001) 599–608, https://doi.org/10.1002/sia.1087.
[51] J.R. Rieken, I.E. Anderson, M.J. Kramer, G.R. Odette, E. Stergar, E. Haney, Reactive gas atomization processing for Fe-based ODS alloys, J. Nucl. Mater. 428 (2012) 65–75, https://doi.org/10.1016/j.jnucmat.2011.08.015.
[52] J.-P. Roth, I. Šulák, T. Kruml, W. Polkowski, T. Dudziak, P. Böhlke, U. Krupp, K. Jahns, establishing a novel process route for additive manufacturing of NiCu-based Alloy 400 – an alignment of gas atomization, laser powder bed fusion and design of experiments, SSRN. https://doi.org/10.2139/ssrn.4537351.
[53] R.L. Meltzer, Y.R. Fiorini, R.T. Horstman, I.C. Moore, A.L. Batik, T. Hostinsky, J. adek, A constant tensile stress creep testing machine, J. Test. Eval. 4 (1976) 26, https://doi.org/10.1520/JTE10503J.
[54] S. Sendino, S. Martinez, A. Lamikiz, Characterization of IN718 recycling powder and its effect on LPBF manufactured parts, Procedia CIRP 94 (2020) 227–232, https://doi.org/10.1016/j.procir.2020.09.043.
[55] J. Sun, M. Guo, K. Shi, D. Gu, Influence of powder morphology on laser absorption behavior and printability of nanoparticle-coated 90W-Ni-Fe powder during laser powder bed fusion, Mater Sci Add Manuf 1 (2022), https://doi.org/10.18063/msam.v1i2.11.
[56] J. Zegzulka, D. Gelnar, L. Jezerska, R. Prokes, J. Rozbroj, Characterization and flowability methods for metal powders, Sci. Rep. 10 (2020) 21004, https://doi.org/10.1038/s41598-020-77974-3.
[57] T. Liu, J.D. Leazer, S.K. Menon, L.N. Brewer, Microstructural analysis of gas atomized Al-Cu alloy feedstock powders for cold spray deposition, Surf. Coating. Technol. 350 (2018) 621–632, https://doi.org/10.1016/j.surfcoat.2018.07.006.
[58] Z. Erdélyi, C. Girardeaux, Z. Tökei, D.L. Beke, C. Cserháti, A. Rolland, Investigation of the interplay of nickel dissolution and copper segregation in Ni/Cu(111) system, Surf. Sci. 496 (2002) 129–140, https://doi.org/10.1016/S0039-6028(01)01571-0.
[59] A.R. Naghash, T.H. Etsell, S. Xu, XRD and XPS study of Cu−Ni interactions on reduced Copper−Nickel−Aluminum oxide solid solution catalysts, Chem. Mater. 18 (2006) 2480–2488, https://doi.org/10.1021/cm051910o.
[60] E. Pellicer, A. Varea, K.M. Sivaraman, S. Pané, S. Suriñach, M.D. Baró, J. Nogués, B. J. Nelson, J. Sort, Grain boundary segregation and interdiffusion effects in nickel-copper alloys: an effective means to improve the thermal stability of nanocrystalline nickel, ACS Appl. Mater. Interfaces 3 (2011) 2265–2274, https://doi.org/10.1021/am2004587.
[61] J. Rieken, I. Anderson, M. Kramer, Innovative Powder Processing of Oxide Dispersion Strengthened ODS Ferritic Stainless Steels, 2011.
[62] J. Rieken, Gas Atomized Precursor Alloy Powder for Oxide Dispersion Strengthened Ferritic Stainless Steel 2011, 2011, https://doi.org/10.2172/1048516.
[63] T. de Terris, O. Andreau, P. Peyre, F. Adamski, I. Koutiri, C. Gorny, C. Dupuy, Optimization and comparison of porosity rate measurement methods of Selective Laser Melted metallic parts, Addit. Manuf. 28 (2019) 802–813, https://doi.org/10.1016/j.addma.2019.05.035.
[64] S. Shrestha, T. Starr, K. Chou, A study of keyhole porosity in selective laser melting: single-track scanning with micro-CT analysis, J. Manuf. Sci. Eng. 141 (2019), https://doi.org/10.1115/1.4043622.
[65] D.S. Ertay, H. Ma, M. Vlasea, Correlative Beam Path and Pore Defect Space Analysis for Modulated Powder Bed Laser Fusion Process, University of Texas at Austin, 2018.
[66] A. Ulbricht, G. Mohr, S.J. Altenburg, S. Oster, C. Maierhofer, G. Bruno, Can potential defects in LPBF Be healed from the laser exposure of subsequent layers? A Quantitative Study, Metals 11 (2021) 1012, https://doi.org/10.3390/met11071012.

[67] T. Hatakeyama, K. Sawada, M. Suzuki, M. Watanabe, Microstructure development of modified 9Cr-1Mo steel during laser powder bed fusion and heat treatment, Addit. Manuf. 61 (2023) 103350, https://doi.org/10.1016/j.addma.2022.103350.
[68] H. Qin, V. Fallah, Q. Dong, M. Brochu, M.R. Daymond, M. Gallerneault, Solidification pattern, microstructure and texture development in Laser Powder Bed Fusion (LPBF) of Al10SiMg alloy, Mater. Char. 145 (2018) 29–38, https://doi.org/10.1016/j.matchar.2018.08.025.
[69] C. Li, R. White, X.Y. Fang, M. Weaver, Y.B. Guo, Microstructure evolution characteristics of Inconel 625 alloy from selective laser melting to heat treatment, Mater. Sci. Eng., A 705 (2017) 20–31, https://doi.org/10.1016/j.msea.2017.08.058.
[70] S. Pilz, T. Gustmann, F. Günther, M. Zimmermann, U. Kühn, A. Gebert, Controlling the Young's modulus of a ß-type Ti-Nb alloy via strong texturing by LPBF, Mater. Des. 216 (2022) 110516, https://doi.org/10.1016/j.matdes.2022.110516.
[71] L. Zou, C. Yang, Y. Lei, D. Zakharov, J.M.K. Wiezorek, D. Su, Q. Yin, J. Li, Z. Liu, E. A. Stach, J.C. Yang, L. Qi, G. Wang, G. Zhou, Dislocation nucleation facilitated by atomic segregation, Nat. Mater. 17 (2018) 56–63, https://doi.org/10.1038/nmat5034.
[72] X.X. Zhang, H. Andrä, S. Harjo, W. Gong, T. Kawasaki, A. Lutz, M. Lahres, Quantifying internal strains, stresses, and dislocation density in additively manufactured AlSi10Mg during loading-unloading-reloading deformation, Mater. Des. 198 (2021) 109339, https://doi.org/10.1016/j.matdes.2020.109339.
[73] T. Voisin, J.-B. Forien, A. Perron, S. Aubry, N. Bertin, A. Samanta, A. Baker, Y. M. Wang, New insights on cellular structures strengthening mechanisms and thermal stability of an austenitic stainless steel fabricated by laser powder-bed-fusion, Acta Mater. 203 (2021) 116476, https://doi.org/10.1016/j.actamat.2020.11.018.
[74] D. Kong, C. Dong, S. Wei, X. Ni, L. Zhang, R. Li, L. Wang, C. Man, X. Li, About metastable cellular structure in additively manufactured austenitic stainless steels, Addit. Manuf. 38 (2021) 101804, https://doi.org/10.1016/j.addma.2020.101804.
[75] K.M. Bertsch, G. Meric de Bellefon, B. Kuehl, D.J. Thoma, Origin of dislocation structures in an additively manufactured austenitic stainless steel 316L, Acta Mater. 199 (2020) 19–33, https://doi.org/10.1016/j.actamat.2020.07.063.
[76] E.B. Clatworthy, S. Yick, A.T. Murdock, M.C. Allison, A. Bendavid, A.F. Masters, T. Maschmeyer, Enhanced photocatalytic hydrogen evolution with TiO 2 –TiN nanoparticle composites, J. Phys. Chem. C 123 (2019) 3740–3749, https://doi.org/10.1021/acs.jpcc.8b09221.
[77] A. Alvarez Barragan, N.V. Ilawe, L. Zhong, B.M. Wong, L. Mangolini, A non-thermal plasma route to plasmonic TiN nanoparticles, J. Phys. Chem. C 121 (2017) 2316–2322, https://doi.org/10.1021/acs.jpcc.6b08910.
[78] U. Guler, S. Suslov, A.V. Kildishev, A. Boltasseva, V.M. Shalaev, Colloidal plasmonic titanium nitride nanoparticles: properties and applications, Nanophotonics 4 (2015) 269–276, https://doi.org/10.1515/nanoph-2015-0017.
[79] J. Tavares, S. Coulombe, J.-L. Meunier, Synthesis of cubic-structured monocrystalline titanium nitride nanoparticles by means of a dual plasma process, J. Phys. D Appl. Phys. 42 (2009) 102001, https://doi.org/10.1088/0022-3727/42/10/102001.
[80] C. Gao, Z. Wang, Z. Xiao, D. You, K. Wong, A.H. Akbarzadeh, Selective laser melting of TiN nanoparticle-reinforced AlSi10Mg composite: microstructural, interfacial, and mechanical properties, J. Mater. Process. Technol. 281 (2020) 116618, https://doi.org/10.1016/j.jmatprotec.2020.116618.
[81] J. Cadek, Creep in metallic materials, in: Materials Science Monographs, 1988.